

Surface encapsulation of layered oxide cathode material with $NiTiO_3$ for enhanced cycling stability of Na-ion batteries

Zilin Hu(胡紫霖), Bin Tang(唐彬), Ting Lin(林挺), Chu Zhang(张楚), Yaoshen Niu(牛耀申), Yuan Liu(刘渊), Like Gao(高立克), Fei Xie(谢飞), Xiaohui Rong(容晓晖), Yaxiang Lu(陆雅翔), and Yongsheng Hu(胡勇胜)
Citation: Chin. Phys. B, 2024, 33 (**8**): 088202. DOI: 10.1088/1674-1056/ad50c2

What follows is a list of articles you may be interested in

Synthesis and electrochemical performance of La_2CuO_4 as a promising coating material for high voltage Li-rich layered oxide cathodes

Fuliang Guo(郭福亮), Jiaze Lu(卢嘉泽), Meihua Su(苏美华), Yue Chen(陈约), Jieyun Zheng(郑杰允), Liang Yin(尹良), and Hong Li(李泓)
Chin. Phys. B, 2023, 32 (**8**): 088201. DOI: 10.1088/1674-1056/acd2bc

Designing a P2-type cathode material with Li in both Na and transition metal layers for Na-ion batteries

Jianxiang Gao(高健翔), Kai Sun(孙凯), Hao Guo(郭浩), Zhengyao Li(李正耀), Jianlin Wang(王建林), Xiaobai Ma(马小柏), Xuedong Bai(白雪东), and Dongfeng Chen(陈东风)
Chin. Phys. B, 2022, 31 (**9**): 098201. DOI: 10.1088/1674-1056/ac6b21

Hard carbons derived from pine nut shells as anode materials for Na-ion batteries

Hao Guo(郭浩), Kai Sun(孙凯), Yaxiang Lu(陆雅翔), Hongliang Wang(王洪亮), Xiaobai Ma(马小柏), Zhengyao Li(李正耀), Yong-Sheng Hu(胡勇胜), Dongfeng Chen(陈东风)
Chin. Phys. B, 2019, 28 (**6**): 068203. DOI: 10.1088/1674-1056/28/6/068203

New layered metal oxides as positive electrode materials for room-temperature sodium-ion batteries

Mu Lin-Qin (穆林沁), Hu Yong-Sheng (胡勇胜), Chen Li-Quan (陈立泉)
Chin. Phys. B, 2015, 24 (**3**): 038202. DOI: 10.1088/1674-1056/24/3/038202

Novel copper redox-based cathode materials for room-temperature sodium-ion batteries

Xu Shu-Yin (徐淑银), Wu Xiao-Yan (吴晓燕), Li Yun-Ming (李云明), Hu Yong-Sheng (胡勇胜), Chen Li-Quan (陈立泉)
Chin. Phys. B, 2014, 23 (**11**): 118202. DOI: 10.1088/1674-1056/23/11/118202

RAPID COMMUNICATION

Surface encapsulation of layered oxide cathode material with $NiTiO_3$ for enhanced cycling stability of Na-ion batteries

Zilin Hu(胡紫霖)[1,2,†], Bin Tang(唐彬)[6,†], Ting Lin(林挺)[5], Chu Zhang(张楚)[1,2], Yaoshen Niu(牛耀申)[1], Yuan Liu(刘渊)[1,2], Like Gao(高立克)[7], Fei Xie(谢飞)[1], Xiaohui Rong(容晓晖)[1,4], Yaxiang Lu(陆雅翔)[1,3,‡], and Yongsheng Hu(胡勇胜)[1,2,3,4,§]

[1] *Key Laboratory for Renewable Energy, Beijing Key Laboratory for New Energy Materials and Devices, Beijing National Laboratory for Condensed Matter Physics, Institute of Physics, Chinese Academy of Sciences, Beijing* 100190, *China*

[2] *College of Materials Science and Optoelectronic Technology, University of Chinese Academy of Sciences, Beijing* 100049, *China*

[3] *Huairou Division, Institute of Physics, Chinese Academy of Sciences, Beijing* 101400, *China*

[4] *Yangtze River Delta Physics Research Center Co. Ltd, Liyang* 213300, *China*

[5] *Beijing National Laboratory for Condensed Matter Physics, Institute of Physics, Chinese Academy of Sciences, Beijing* 100049, *China*

[6] *Yangtze River Delta Physics Research Center Co. Ltd, Liyang* 213300, *China*

[7] *Guangxi Power Grid Co. Ltd., Nanning* 530023, *China*

(Received 16 April 2024; revised manuscript received 7 May 2024; accepted manuscript online 28 May 2024)

In Na-ion batteries, O3-type layered oxide cathode materials encounter challenges such as particle cracking, oxygen loss, electrolyte side reactions, and multi-phase transitions during the charge/discharge process. This study focuses on surface coating with $NiTiO_3$ achieved via secondary heat treatment using a coating precursor and the surface material. Through *in-situ* x-ray diffraction (XRD) and differential electrochemical mass spectrometry (DEMS), along with crystal structure characterizations of post-cycling materials, it was determined that the $NiTiO_3$ coating layer facilitates the formation of a stable lattice structure, effectively inhibiting lattice oxygen loss and reducing side reaction with the electrolyte. This enhancement in cycling stability was evidenced by a capacity retention of approximately 74% over 300 cycles at 1 C, marking a significant 30% improvement over the initial sample. Furthermore, notable advancements in rate performance were observed. Experimental results indicate that a stable and robust surface structure substantially enhances the overall stability of the bulk phase, presenting a novel approach for designing layered oxide cathodes with higher energy density.

Keywords: Na-ion battery, layered oxides, high voltage, surface coating

PACS: 82.47.Aa, 82.45.Fk **DOI:** 10.1088/1674-1056/ad50c2

1. Introduction

The rising demand for energy coupled with increasing environmental concerns has spurred the development of large-scale energy storage technologies. However, the limited availability and uneven distribution of lithium resources have hindered the widespread adoption of lithium-ion batteries in large-scale storage. In response, Na-ion batteries have emerged as a promising alternative due to their abundant sodium resources and lower cost.[1–3] O3-type layered oxide cathode materials garnered significant attention from researchers because of their inherent advantages, including high specific capacity and facile preparation, rendering them highly promising for various applications.[4–6] However, challenges such as irreversible phase transition and lattice oxygen loss in layered oxides are exacerbated at high cut-off voltages, leading to accelerated structural degradation and deterioration of electrochemical performance.[7–10] Meanwhile, certain commonly employed carbonate electrolytes exhibit thermodynamic instability when the voltage exceeds 4.0 V.[11,12] The continuous decomposition of the electrolyte leads to an escalation of the interfacial impedance[13] and ongoing capacity degradation. Therefore, establishing a stable cathode/electrolyte interface (CEI) is crucial for achieving stable cycling at high voltages in Na-ion batteries.

Surface coating technology involves the fabrication of artificial CEI films on the material surface. Various materials, including metal oxides (e.g., Al_2O_3,[14] TiO_2,[15] and MgO[16]), metal fluorides,[17] solid-state electrolytes,[18–20] and organic polymers,[21] have been progressively utilized in the coating applications for the cathode materials. These coating materials effectively preserve the stability of the phase transition of cathode materials throughout the charging and discharging process. Additionally, they effectively mitigate the occurrence of side reactions between cathode materials and electrolyte, suppress erosion of cathode materials caused by byproducts such as HF, and enhance Na^+ transport pathways. Consequently, these coating layers can substantially improve the cycling stability. Furthermore, the presence of the coating layer enables effective isolation of the material from atmospheric

[†]These authors contributed equally to this work.

[‡]Corresponding author. E-mail: yxlu@iphy.ac.cn

[§]Corresponding author. E-mail: yshu@iphy.ac.cn

© 2024 Chinese Physical Society and IOP Publishing Ltd

conditions, thereby significantly enhancing the air stability of cathode materials.[22]

Perovskite compounds, owing to their structural resemblance to layered oxides, demonstrate exceptional compatibility and robust bonding, thus showing significant potential for coherent growth. In recent years, there has been a proliferation of studies investigating the incorporation of perovskite materials as coating layer or doping phases into layered-structure materials. These studies have demonstrated promising outcomes in enhancing the cycling stability of lithium-ion batteries, particularly under high-voltage conditions. By incorporating the perovskite-structured La_4LiTMO_8 (TM = Ni, Co, Mn) coherent phase as an anchoring component within the lithium nickel-rich cathodes, lattice strain in the layered oxides during charge–discharge processes is effectively mitigated, enabling stable cycling even at exceptionally high cutoff voltages of up to 4.6 V.[23] The perovskite structure of La_4NiLiO_8 possesses a significant number of oxygen vacancies, facilitating the capture of active oxygen species. When used as an oxygen reservoir layer coated onto $LiNi_{0.9}Co_{0.05}Mn_{0.05}O_2$, La_4NiLiO_8 effectively suppresses the oxygen release, mitigates irreversible phase transitions, and minimizes side reactions with the electrolyte, thereby enhancing long-term capacity retention in nickel-rich layered cathode materials.[24] Furthermore, perovskite phase compounds function as coating layers in lithium cobalt oxide and lithium-rich materials, thereby effectively improving the cycling performance and enhancing rate capability.[25,26]

Current efforts in utilizing perovskite compounds for Na-ion batteries are primarily concentrated on the developing of high-performance anode materials, such as $NiTiO_3$ and $CoTiO_3$.[27,28] Previous studies have demonstrated that the appearance of NiO heterogeneous phases in nickel-rich Na-ion battery layered oxides following secondary heat treatment is a precipitation phenomenon resulting from the reduction in solid solubility of Ni caused by sodium volatilization during the heating process.[29,30] Moreover, $NiTiO_3$ with perovskite structure exhibits excellent compatibility with layered structures and demonstrates outstanding electrochemical stability as a negative electrode material for Na-ion batteries. In this study, we initially obtain TiO_2-coated cathode materials through the hydrolysis reaction of titanium isopropoxide (TTIP), followed by a secondary heat treatment that facilitates the reaction with precipitated NiO in these materials, resulting in the formation of a $NiTiO_3$ coating on the surface of the cathode material. Experimental results demonstrate that the $NiTiO_3$ coating layer facilitates the establishment of a stable lattice structure, effectively suppresses the release of the oxygen, and mitigates the side reactions between the material and electrolyte, thereby significantly enhancing the electrochemical performance of the $NiTiO_3$-coated materials.

2. Experimental details

2.1. Material synthesis

$NaLi_{0.05}Ni_{0.375}Fe_{0.1}Mn_{0.375}Ti_{0.1}O_2$ (P-LNFMT) was prepared by a simple solid-state reaction using precursors of Na_2CO_3 (99.5%, Alfa), $LiOH{\cdot}H_2O$ (98%, Alfa), NiO (99.9%, Alfa), Fe_2O_3 (99.9%, Alfa), MnO_2 (99.9%, Alfa) and TiO_2 (99.9%, Alfa). The starting materials were mixed thoroughly in an agate mortar and then calcined at 900 °C for 15 h.

Then 2% $NiTiO_3$–$NaLi_{0.05}Ni_{0.375}Fe_{0.1}Mn_{0.375}Ti_{0.1}O_2$ (NTO-LNFMT) was prepared using the secondary heat treatment approach. The anhydrous ethanol with titanium isopropoxide (TTIP) was stirred in a beaker for 5 min. Then, P-LNFMT was added to the alcohol solution and stirred at room temperature for 60 min. The mixture was heated and stirred at 80 °C until the ethanol was completely volatilized. Subsequently, the powder was secondarily sintered at 1000 °C for 4 h. Finally, the sample of NTO-LNFMT was obtained.

2.2. Electrochemical measurements

The cathodes were prepared by mixing active material, conductive carbon black (super P), and polyvinylidene fluoride (PVDF) binder at a weight rate of 8:1:1 in N-methyl-2-pyrrolidone (NMP) solvent. The slurry was then cast onto an Al foil and dried at 120 °C for 6 h under a vacuum to obtain the electrodes. The loading mass of the active materials is approximately 5 $mg{\cdot}cm^{-2}$. The electrochemical performance was assessed by coin-type (CR2032) half cells using sodium metal as the anode in an argon-filled glove box ($H_2O \leq 0.1$ ppm, $O_2 \leq 0.1$ ppm). A glass fiber (diameter: 16.2 mm) was used as the separator, and 1 M $NaClO_4$ in propylene carbonate (PC) with fluoroethylene carbonate (2% in volume) was used as the electrolyte. The charge and discharge measurements for the half cells were carried out on a Land CT2001A battery test system in the voltage ranges of 2.0 V–4.3 V, and cyclic voltammetry (CV) tests were performed at 0.1 $mV{\cdot}s^{-1}$ scan rates in the voltage range of 2.0 V–4.3 V vs. Na^+/Na on an electrochemical workstation CHI 604E. Both tests were carried out at room temperature.

2.3. Material characterizations

The crystal structures of the as-prepared samples were analyzed using powder x-ray diffraction (XRD), which employed the Bruker D8 ADVANCE instrument with a Cu K_α x-ray source ($\lambda_1 = 1.54060$ Å and $\lambda_2 = 1.54439$ Å). The actual chemical composition of the obtained cathode materials was analyzed by inductively coupled plasma-atomic emission spectroscopy (ICP-AES, Shimadzu, ICPS-8100).

SEM measurements were carried out using a Hitachi S-4800 (10 kV). STEM observation and high-angle toroidal dark field (HAADF) image were obtained for the analysis of the microstructure of the material using a JEOL ARM200CF trans-

mission electron microscope equipped with double aberration correctors and objective lens, with a HAADF receiving angle of 90 mrad–370 mrad. The electron energy loss spectroscopy (EELS) of the O *K*-edge and the *L*-edge of Ni, Fe, Mn, and Ti was obtained using STEM-EELS in dual EELS mode with an acceleration voltage of 200 keV.

A self-made *in-situ* battery shell was used for differential electrochemical mass spectrometry (DEMS) testing to monitor the gas production of the battery.

A gas chromatography-mass spectrometry (GC-MS, Agilent 7890B/5977A) detector was used for gas collection. The test voltage range for *in-situ* testing was 2.0 V–4.3 V, and the current density was 16 $mA{\cdot}g^{-1}$.

Differential scanning calorimetry (DSC) measurements were conducted by DSC 214 Polyma (Netzsch) under Ar atmosphere at a temperature scan rate of 5 $°C{\cdot}min^{-1}$.

2.4. DFT methods

Density-functional theory (DFT) calculations were performed using the projector augmented wave (PAW)[31] method by the Vienna *ab initio simulation* package (VASP).[32] The exchange–correlation function was conducted by the spin-polarized generalized gradient approximation (GGA) with the Perdew–Burke–Ernzerhof (PBE)[33] functional in combination with Hubbard U corrections (GGA-PBE + U). Hubbard U type correction was adopted with an effective U value of 3.9 eV for Mn.[34] The cut-off energy, the convergences of the total energy and residual force were set to 500 eV, 10^{-4} eV, and 0.02 $eV{\cdot}Å^{-1}$, respectively. The formation energy of oxygen vacancy ($E_{\text{oxygen vacancy formation}}$) was calculated according to the following equation:

$$E_{\text{oxygen vacancy formation}} = E_{\text{sample-O}} + 0.5E(O_2) - E_{\text{sample}}.$$

Here, E_{sample} and $E_{\text{sample-O}}$ represent the total energy of the system before and after losing one oxygen atom.

3. Results and discussion

As shown in Figs. 1(a) and 1(b), both P-LNFMT and NTO-LNFMT exhibit a typical α-$NaFeO_2$ structure, belonging to the space group of $R\bar{3}m$, without any discernible impurity peaks. XRD refinement result reveals that compared to P-LNFMT (c = 15.9810 Å), the interslab distance of NTO-LNFMT increases (c = 16.08040 Å), which implies that the NTO coating can broaden the Na^+ diffusion channel thus enhancing the rate performance of the material.[35] Figures 1(c) and 1(e) show that both materials possess similar lamellar morphology with particle sizes ranging from 2 μm to 4 μm. However, fine dotted coating layers are observed on the surface of NTO-LNFMT. For further study on the microstructure of the coating layer, a spherical aberration-corrected scanning transmission electron microscope (STEM) was used to observe the structural changes of the samples before and after coating. As depicted in Fig. 1(d), P-LNFMT exhibits a layered structure extending from the bulk to the surface. In contrast, the surface structure of NTO-LNFMT notably deviates from that of the bulk (Fig. 1(f)). A coating layer (∼ 6 nm) exists on the surface of NTO-LNFMT and the atomic arrangement of the coating layer aligns with the $[001]_L$ projection of NTO (Fig. 1(h)).[36,37]

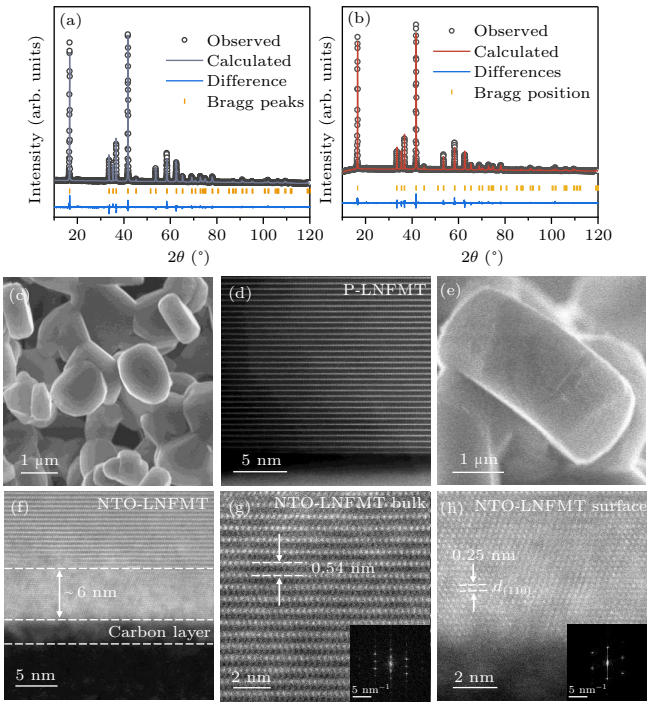


Fig. 1. Structural characterizations of P-LNFMT and NTO-LNFMT. The XRD Rietveld refinement patterns of P-LNFMT (a) and NTO-LNFMT (b); the SEM images of P-LNFMT (c) and NTO-LNFMT (e); the HAADF images of the P-LNFMT (d) and NTO-LNFMT after focused-ion-beam (FIB) treatment (f) in [100] zone projection. The enlarged HAADF images of FIB-treated NTO-LNFMT in the bulk (g) and near the surface (h). The corresponding FFT images are shown as the insets in panels (g) and (h).

The elemental distribution of NTO-LNFMT's surface cladding was analyzed using electron energy loss spectra (EELS) and the regions A and B in Fig. 2(a) represent the acquisition areas. The EELS mapping results are shown in Fig. 2(b), where the elements Fe and Mn are distributed only in the B region, corresponding to the bulk region of the material. The elements Ni, Ti, and O are distributed in both the A and B regions, which indicates that these three elements are distributed in both the bulk and surface of the material. Moreover, for the Ti element, there is an obvious enrichment in the region of ∼ 6 nm on the surface, which is consistent with the thickness of the coating layer in Fig. 1(h). It suggests that the enrichment of Ti may be caused by the significantly higher Ti content of NTO than that in the designed P-LNFMT. In summary, NTO was successfully introduced into the material surface.

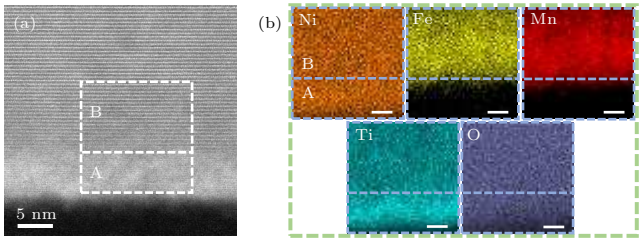


Fig. 2. The HAADF image of NTO-LNFMT after FIB treatment (a) in [100] zone projection and the EELS mapping images of the area surrounded by white lines (b, the scale bar is 2 nm).

The electrochemical performance of P-LNFMT and NTO-LNFMT was compared within the voltage range of 2.0 V to 4.3 V (Fig. 3). As illustrated in Fig. 3(a), the NTO-LNFMT cathode shows a higher reversible capacity ($\sim$ 180 mAh·g^{-1}) than that of P-LNFMT ($\sim$ 176 mAh·g^{-1}) at 0.1 C (0.1 C = 16 mA·g^{-1}) in the first cycle, along with an improved initial coulombic efficiency (ICE) from $\sim$ 86% to $\sim$ 92%. Voltage profiles indicate that the improvement of ICE primarily stems from the reduction of the irreversible plateau above 4.1 V. The long plateau in the high-voltage region is typically attributed to irreversible phase transitions, surface residual alkali decomposition, and side reactions between the cathode and the electrolyte.[38] The comparison of the 1st and 10th voltage profiles demonstrates that the decay of the charging and discharging platforms in the low-voltage region below 3.0 V is the primary cause of capacity degradation, as well as in the high-voltage region above 4.1 V. These findings are further supported by cyclic voltammetry (CV) curves (Fig. 3(b)). After 300 cycles at a current density of 160 mA·g^{-1}, NTO-LNFMT exhibits enhanced cycling stability with an impressive capacity retention rate of approximately 74%, while P-LNFMT retains only about 44% of its initial capacity under identical testing conditions (Fig. 3(d)). Additionally, the rate performance of NTO-LNFMT has been significantly improved (Fig. 3(c)). The reversible specific capacity of NTO-LNFMT reaches $\sim$ 125 mAh·g^{-1} at 5 C, whereas P-LNFMT achieves only 104 mAh·g^{-1}. These combined observations indicate that the NTO coating layer not only serves as an interfacial film to reduce side reactions between the cathode and electrolyte, but also enhances the structural stability.[28]

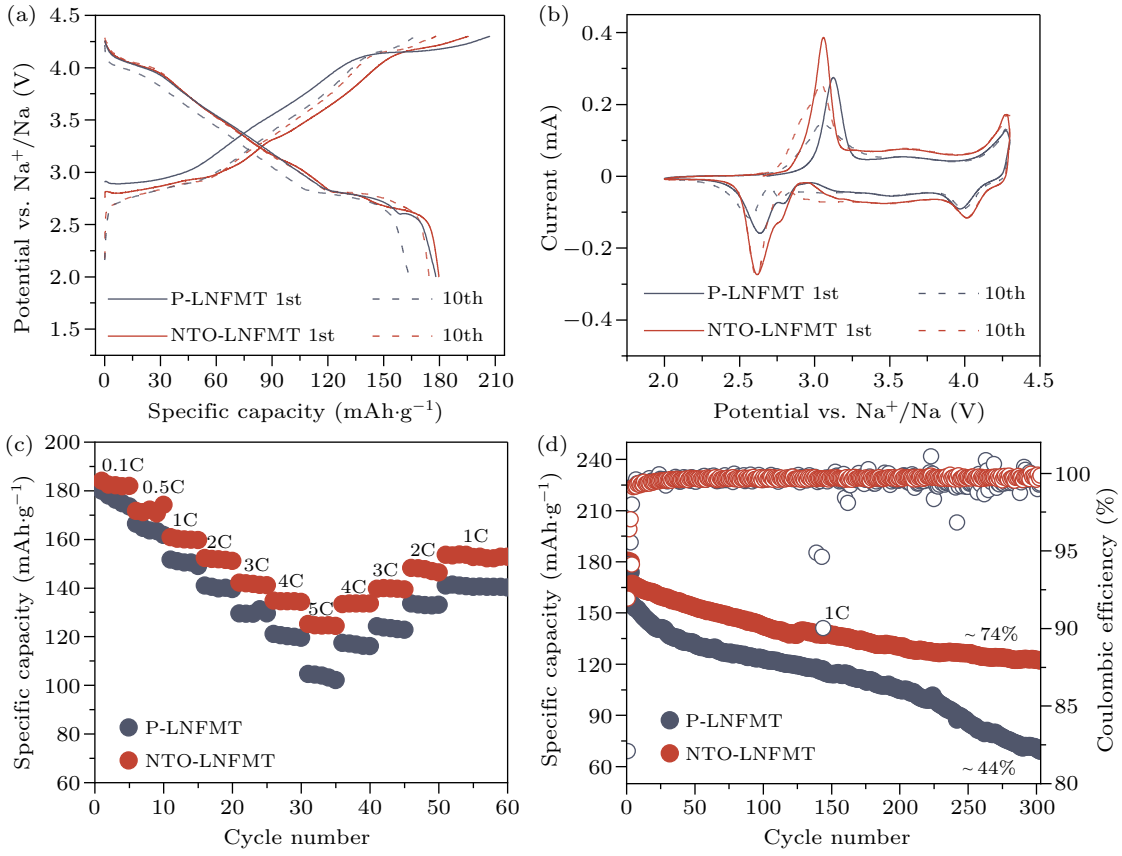


Fig. 3. The 1st and 10th voltage profiles of P-LNFMT and NTO-LNFMT between 2.0 V and 4.3 V (a); the CV profiles in the initial two cycles (b); the rate performance (c) and the cycling performance profiles (d).

The O3-type layered oxide cathode materials tend to undergo multiple phase transitions during the charging and discharging process. The huge volume deformation can lead to structural fatigue and damage to the materials, thus reducing their cycling stability.[39,40] To further investigate the effect of NTO coating on the phase transition and structural evolution of the materials, *in-situ* XRD analysis was conducted for P-LNFMT and NTO-LNFMT. Figure 4 shows that P-LNFMT

and NTO-LNFMT undergo a similar O3–P3–OP2 phase transition process. It is noteworthy that the (002) diffraction peak of the OP2 phase exhibits a pronounced shift towards higher angles upon further charging beyond 4.2 V (Fig. 4(a)). When the Na content of materials is approximately lower than 0.3, the interslab distance decreases dramatically, resulting in a collapse of the material structure. This phenomenon can also explain why the cycling stability of the O3-type material significantly decreases at cut-off voltages higher than 4.0 V. The 2D contour maps of the (003) diffraction peaks and the statistical maps of the variation in interslab distance for P-LNFMT and NTO-LNFMT are shown in Figs. 4(b) and 4(c), respectively. Compared to the initial O3 structure, the (003) diffraction peak of P-LNFMT shifts by 0.508° upon charging to 4.3 V, while NTO-LNFMT shows a smaller shift of 0.412°. This indicates that NTO-LNFMT undergoes fewer structural changes during the charging process. In the voltage range of 2.0 V–4.05 V, the interslab distance of the two materials is changed by only about 6%, which is related to the phase transitions of O3–P3. However, when charged to higher than 4.05 V, both materials experience a more complicated phase change from P3 to OP2, resulting in significant contraction along the *c*-axis and potentially causing large volume changes and loss of crystallinity,[41–43] thereby negatively impacting the cycling stability of the materials.

Although the material still exhibits *c*-axis contraction after NTO encapsulation, it is worth noting that compared to the initial O3 structure, the interplanar spacing of NTO-LNFMT contracts by 8.9% when charged to 4.3 V, which is lower than P-LNFMT's contraction of 9.5%. This indicates that NTO encapsulation can play a certain role in suppressing phase transition and prolonging the cycling lifespan of the material.

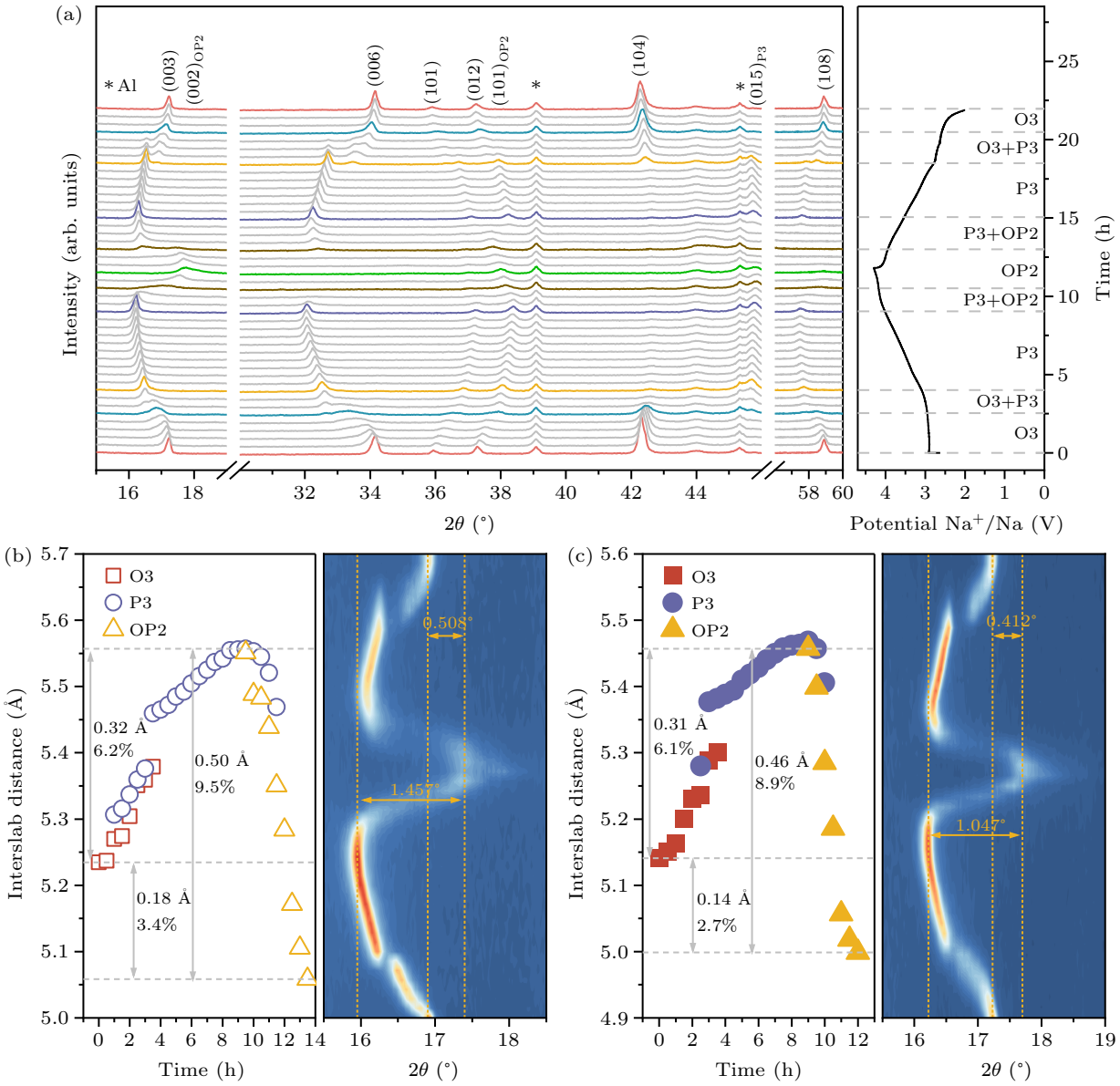


Fig. 4. *In-situ* XRD contour plots of (003) for P-LNFMT (a) and NTO-LNFMT (c); lattice parameters (interslab distance) during the initial cycle process for the P-LNFMT (b) and NTO-LNFMT (c) electrodes.

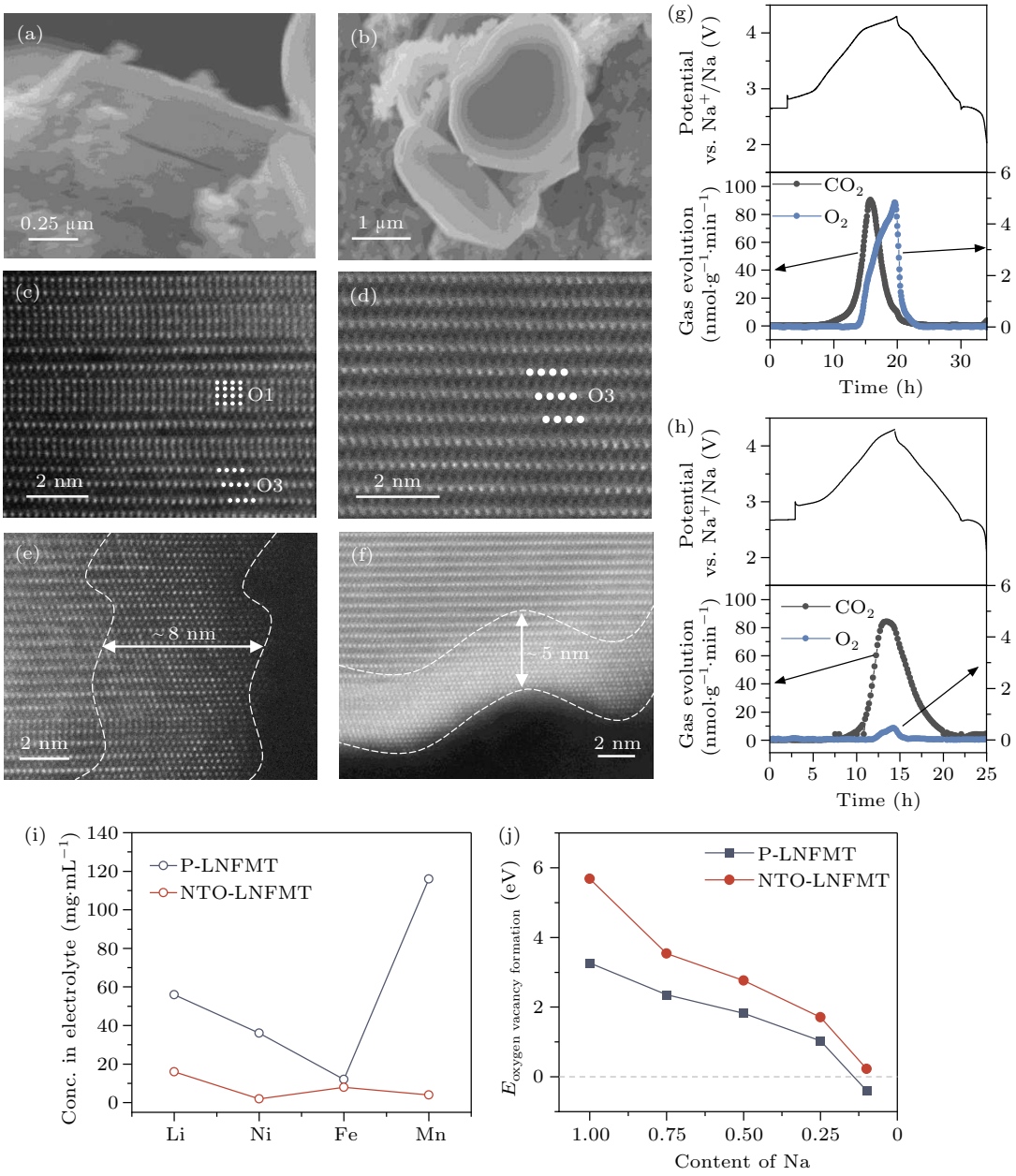


Fig. 5. The SEM images (a) and (b) and HADDF-STEM images [bulk: (c), (d); surface: (e), (f)] of P-LNFMT [(a), (c), (e)] and NTO-LNFMT [(b), (d), (f)] after 200 cycles within the voltage range of 2.0 V–4.3 V at 1 C; gas evolution detected by *in-situ* DEMS of P-LNFMT (g) and NTO-LNFMT (h); dissolved Li, Ni, Fe and Mn in the electrolytes measured by ICP-AES after 200 cycles at 1 C (i); the oxygen vacancy formation energy of P-LNFMT and NTO-LNFMT (j).

Previous studies have shown that structure degradation often initiates at the particle surface and gradually diffuses into the bulk phase.[30,42–44] Therefore, establishing a robust surface structure is frequently effective in preventing the deterioration of the bulk structure. More detailed characterizations of P-LNFMT and NTO-LNFMT after 200 cycles at 1 C were carried out to investigate the underlying mechanism of enhanced cycling stability by NTO coating.

After 200 cycles, the particles of P-LNFMT crack due to excessive internal stress caused by volumetric deformation during the charging and discharging process (Fig. 5(a)).[45,46] Figure 5(b) shows that the surface of NTO-LNFMT particles was intact, indicating that the NTO coating can play a role in reducing the volumetric deformation. Figure 5(c) shows a large number of O1 structures in the cycled P-LNFMT. Combining the results of *in-situ* XRD, the irreversible phase transition in the high voltage region leads to the residual O1 structure, which progressively accumulates throughout subsequent cycles and consequently leads to a rapid capacity decline. Moreover, a thick reconstruction layer of approximately 8 nm on the surface of P-LNFMT inhibits the insertion of Na^+ and results in increased polarization (Fig. 5(e)).[45] In contrast, the structure of the long-cycled NTO-LNFMT material remains intact, with the thickness of the NTO coating layer on the surface remaining at approximately 5 nm (Figs. 5(d) and 5(f)).

The severe surface reconstruction indicates that the mate-

rial undergoes significant oxygen loss and transition metal migration during the cycling, intensifying the dissolution of the transition metal.[47] *In-situ* differential electrochemical mass spectrometry (DEMS) was employed to study gas evolution during the first cycle. Figures 5(g) and 5(h) show significantly less O_2 evolution in NTO-LNFMT compared to P-LNFMT. Moreover, the oxygen vacancy formation energy at different Na content was calculated by DFT. The results showed that the $E_{\text{oxygen vacancy formation}}$ values of NTO-LNFMT are always higher than those of P-LNFMT with the removal rate of Na^+, which demonstrates the high stability of lattice oxygen of NTO-LNFMT (Fig. 5(j)). Additionally, the dissolution of transition metal leads to prominent capacity decay of layered cathodes.[47] The transition metal content in the cycled electrolyte by ICP-AES (Fig. 5(i)) reveals that the NTO coating significantly suppressed the dissolution of transition metals and improved the cycling stability of the material.

Full coin-type cells with the NTO-LNFMT cathode and hard carbon (HC) anode were assembled to evaluate the long-term cycling stability and practical application value of the cathode. As shown in Fig. 6(a), the full cell delivered a high reversible specific capacity of 170 $mAh{\cdot}g^{-1}$ (based on the active material of the cathode) within the voltage range of 1.0 V–4.3 V at 0.1 C. After 200 cycles at 0.5 C, the capacity retention was 84%, which is superior to that observed in half-cells and shows very promising potential for practical applications (Fig. 6(c)). Based on the total mass of active materials, the energy density obtained from this matched full cell is 329 $Wh{\cdot}kg^{-1}$. This excellent electrochemical performance can promote the application of the NTO-LNFMT full cell in Na-ion batteries for large-scale energy.

Furthermore, the thermal stability of the material in the charging state is a crucial safety indicator in Na-ion battery testing.[48] Differential scanning calorimetry (DSC) as an effective thermal analysis technique is commonly used to test the thermal stability of materials. To replicate the fully charged battery system, P-LNFMT and NTO-LNFMT were subjected to testing after charged to 4.3 V in the presence of electrolyte ($m_{\text{electrolyte}} : m_{\text{cathode}} = 1 : 1$). The exothermal peak can be attributed to the oxygen loss and the reduction of transition metals during the heating process (Fig. 6(b)), accompanied by the phase transition and significant release of heat.[49] The exothermal peak of P-LNFMT is located at 298.1 °C with a heat generation of 599.2 $J{\cdot}g^{-1}$, while NTO-LNFMT displays an exothermal peak at a significantly higher temperature (304.5 °C), and overall heat generation is reduced to 320.8 $J{\cdot}g^{-1}$. It can be noticed that the exothermal peak of NTO-LNFMT tends to split into two peaks, which may be attributed to uneven contact between the electrode and the crucible bottom.

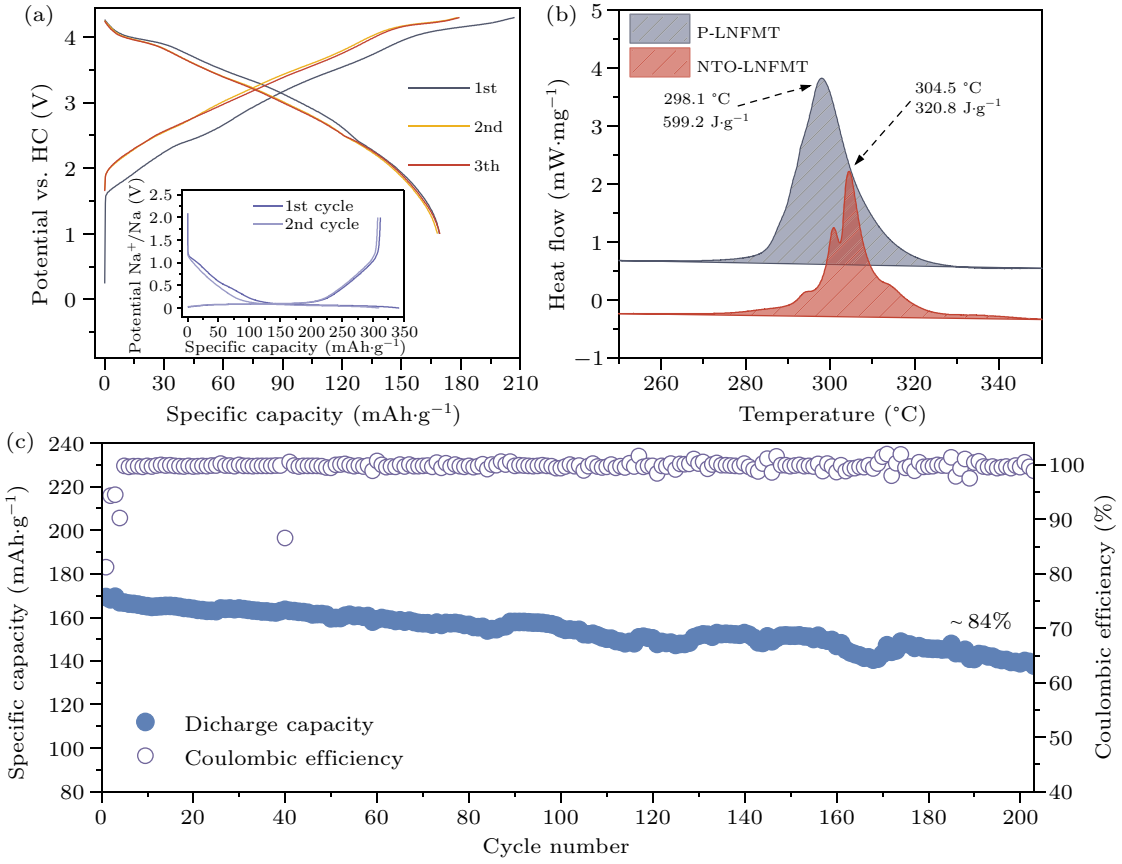


Fig. 6. The voltage profiles (a) and cycling performance (c) of NTO-LNFMT//HC full cell, the inset in panel (a) is the voltage profiles of HC anode; DSC profiles of P-LNFMT and NTO-LNFMT cathode materials charged to 4.3 V with a heating rate of 5 $°C{\cdot}min^{-1}$ (b).

4. Conclusion and perspectives

In conclusion, a novel *in-situ* chemical reaction strategy was employed to achieve NTO coatings coordinated with the lattice on layered oxide particles. The $NiTiO_3$ coating layer facilitates the stabilization of the lattice structure and inhibits the loss of lattice oxygen, dissolution of transition metals, irreversible phase transitions, particle cracking, and side reactions between the cathode material and the electrolyte. As a result, NTO-LNFMT-based cells achieve significantly improved long-term cycling capability and excellent rate performance, even with ultra-high cut-off voltage (4.3 V vs. Na^+/Na). This chemically reaction-driven lattice phase-coordinated interface has excellent potential for application in layered oxide materials. It is well adapted to the higher energy density requirements of Na-ion batteries. Moreover, a profound understanding of the growth mechanism of this unique phase will provide a new perspective for the rational design of surface coating layers in high-energy-density electrode materials.

Acknowledgments

Project supported by the National Key R&D Program of China (Grant No. 2022YFB2402500), the National Natural Science Foundation of China (Grant Nos. 52122214, 92372116, and 52394174), Youth Innovation Promotion Association of the Chinese Academy of Sciences (Grant No. 2020006), Jiangsu Province Carbon Peak and Neutrality Innovation Program (Industry tackling on prospect and key technology BE2022002-5), and Guangxi Power Grid Project (Grant No. GXKJXM20210260).

References

[1] Song S, Kotobuki M, Chen Y, Manzhos S, Xu C, Hu N and Lu L 2017 *Sci. Rep.* **7** 373
[2] Yabuuchi N, Kubota K, Dahbi M and Komaba S 2014 *Chem. Rev.* **114** 11636
[3] Gao J, Sun K, Guo H, Li Z, Wang J, Ma X, Bai X and Chen D 2022 *Chin. Phys. B* **31** 098201
[4] Xi K, Chu S, Zhang X, Zhang X, Zhang H, Xu H, Bian J, Fang T, Guo S, Liu P, Chen M and Zhou H 2020 *Nano Energy* **67** 104215
[5] Zhao C, Lu Y, Chen L and Hu Y S 2019 *Nano Res.* **12** 2018
[6] Ding Y, Ding F, Rong X, Lu Y and Hu Y S 2022 *Chin. Phys. B* **31** 068201
[7] Wang P F, Yao H R, Liu X Y, Yin Y X, Zhang J N, Wen Y, Yu X, Gu L and Guo Y G 2018 *Sci. Adv.* **4** eaar6018
[8] Sathiya M, Jacquet Q, Doublet M L, Karakulina O M, Hadermann J and Tarascon J-M 2018 *Adv. Energy Mater.* **8** 1702599
[9] Hwang J Y, Oh S M, Myung S T, Chung K Y, Belharouak I and Sun Y K 2015 *Nat. Commun.* **6** 6865
[10] Guo Y J, Wang P F, Niu Y B, Zhang X D, Li Q, Yu X, Fan M, Chen W P, Yu Y, Liu X, Meng Q, Xin S, Yin Y X and Guo Y G 2021 *Nat. Commun.* **12** 5267
[11] You Y and Manthiram A 2017 *Adv. Energy Mater.* **8** 1701785
[12] Goodenough J B and Kim Y 2010 *Chem. Mater.* **22** 587
[13] Lee E, Brown D E, Alp E E, Ren Y, Lu J, Woo J J and Johnson C S 2015 *Chem. Mater.* **27** 6755
[14] Liu Y, Fang X, Zhang A, Shen C, Liu Q, Enaya H A and Zhou C 2016 *Nano Energy* **27** 27
[15] Yu Y, Kong W, Li Q, Ning D, Schuck G, Schumacher G, Su C and Liu X 2020 *ACS Appl. Energy Mater.* **3** 933
[16] Ramasamy H V, Kaliyappan K, Thangavel R, Aravindan V, Kang K, Kim D U, Park Y I, Sun X and Lee Y S 2017 *J. Mater. Chem. A* **5** 13842
[17] Zhou Y, Lee Y, Sun H, Wallas J M, George S M and Xie M 2017 *ACS Appl. Mater. Inter.* **9** 9614
[18] Tan Z, Chen X, Li Y, Xi X, Hao S, Li X, Shen X, He Z, Zhao W and Yang Y 2023 *Adv. Funct. Mater.* **33** 2215123
[19] Jo J H, Choi J U, Konarov A, Yashiro H, Yuan S, Shi L, Sun Y K and Myung S T 2018 *Adv. Funct. Mater.* **28** 1705968
[20] Jo C H, Jo J H, Yashiro H, Kim S J, Sun Y K and Myung S T 2018 *Adv. Energy Mater.* **8** 1702942
[21] Yang H, Gao R M, Zhang X D, Liang J Y, Meng X H, Lu Z Y, Cao F F and Ye H 2022 *Adv. Mater.* **34** e2204835
[22] Wang H, Ding F, Wang Y, Han Z, Dang R, Yu H, Yang Y, Chen Z, Li Y, Xie F, Zhang S, Zhang H, Song D, Rong X, Zhang L, Xu J, Yin W, Lu Y, Xiao R, Su D, Chen L and Hu Y S 2023 *ACS Energy Lett.* **8** 1434
[23] Wang L, Liu T, Wu T and Lu J 2022 *Nature* **611** 61
[24] Wang L, Liu G, Wang R, Wang X, Wang L, Yao Z, Zhan C and Lu J 2023 *Adv. Mater.* **35** 2209483
[25] Gao M, Yan C, Shao Q, Chen J, Zhang C, Chen G, Jiang Y, Zhu T, Sun W, Liu Y, Gao M and Pan H 2021 *Small* **17** 2008132
[26] Cai M, Dong Y, Xie M, Dong W, Dong C, Dai P, Zhang H, Wang X, Sun X, Zhang S, Yoon M, Xu H, Ge Y, Li J and Huang F 2023 *Nat. Energy* **8** 159
[27] Tang Y, Wu L, Xiao L, Wen D, Guo Q and Liang W 2018 *Ceram. Int.* **44** 18025
[28] Majumder T, Das D and Majumder S B 2021 *Mater. Lett.* **301** 130293
[29] Yang H, Zhang Q, Chen M, Yang Y and Zhao J 2023 *Adv. Funct. Mater.* **34** 2308257
[30] Ding F, Zhao C, Zhou D, Meng Q, Xiao D, Zhang Q, Niu Y, Li Y, Rong X, Lu Y, Chen L and Hu Y S 2020 *Energy Storage Mater.* **30** 420
[31] Blöchl P E 1994 *Phys. Rev. B* **50** 17953
[32] Kresse G and Furthmüller J 1996 *Comp. Mater. Sci.* **6** 15
[33] Perdew J P, Burke K and Ernzerhof M 1996 *Phys. Rev. Lett.* **77** 3865
[34] Wang L, Maxisch T and Ceder G 2006 *Phys. Rev. B* **73** 195107
[35] Shi Q, Qi R, Feng X, Wang J, Li Y, Yao Z, Wang X, Li Q, Lu X, Zhang J and Zhao Y 2022 *Nat. Commun.* **13** 3205
[36] Li M W, Yuan J P, Gao X M, Liang E Q and Wang C Y 2016 *Appl. Phys. A* **122** 725
[37] Paramanik L, Subudhi S and Parida K M 2022 *Mater. Res. Bull.* **155** 111965
[38] Xu W, Dang R, Zhou L, Yang Y, Lin T, Guo Q, Xie F, Hu Z, Ding F, Liu Y, Liu Y, Mao H, Hong J, Zuo Z, Wang X, Yang R, Jin X, Lu Y, Rong X, Xu N and Hu Y S 2023 *Adv. Mater.* **35** e2301314
[39] Ding W, Ren H, Li Z, Shang M, Song Y, Zhao W, Chang L, Pang T, Xu S, Yi H, Zhou L, Lin H, Zhao Q and Pan F 2024 *Adv. Energy Mater.* **14** 2303926
[40] Yoda Y, Kubota K, Kuroki K, Suzuki S, Yamanaka K, Yaji T, Amagasa S, Yamada Y, Ohta T and Komaba S2020 *Small* **16** e2006483
[41] Niu Y, Hu Z, Zhang B, Xiao D, Mao H, Zhou L, Ding F, Liu Y, Yang Y, Xu J, Yin W, Zhang N, Li Z, Yu X, Hu H, Lu Y, Rong X, Li J and Hu Y S 2023 *Adv. Energy Mater.* **13** 2300746
[42] Mariyappan S, Marchandier T, Rabuel F, Iadecola A, Rousse G, Morozov A V, Abakumov A M and Tarascon J M 2020 *Chem. Mater.* **32** 1657
[43] Wang Q, Mariyappan S, Vergnet J, Abakumov A M, Rousse G, Rabuel F, Chakir M and Tarascon J M 2019 *Adv. Energy Mater.* **9** 1901785
[44] Zheng J, Gu M, Xiao J, Zuo P, Wang C and Zhang J G 2013 *Nano Lett.* **13** 3824
[45] Zhang H, Omenya F, Yan P, Luo L, Whittingham M S, Wang C and Zhou G 2017 *ACS Energy Lett.* **2** 2607
[46] Du X Y, Meng Y, Yuan H and Xiao D 2023 *Energy Storage Mater.* **56** 132
[47] Zhang K, Xu Z, Li G, Luo R J, Ma C, Wang Y, Zhou Y N and Xia Y 2023 *Adv. Energy Mater.* **13** 2302793
[48] Yang X, Wang C, Yan P, Jiao T, Hao J, Jiang Y, Ren F, Zhang W, Zheng J, Cheng Y, Wang X, Yang W, Zhu J, Pan S, Lin M, Zeng L, Gong Z, Li J and Yang Y 2022 *Adv. Energy Mater.* **12** 2200197
[49] Ding F, Zhao C, Xiao D, Rong X, Wang H, Li Y, Yang Y, Lu Y and Hu Y S 2022 *J. Am. Chem. Soc.* **144** 8286